

Study of material homogeneity in the long fiber thermoset injection molding process by image texture analysis

Robert Maertens, Ludwig Schöttl, Wilfried V. Liebig, Peter Elsner & Kay A. Weidenmann

To cite this article: Robert Maertens, Ludwig Schöttl, Wilfried V. Liebig, Peter Elsner & Kay A. Weidenmann (2022) Study of material homogeneity in the long fiber thermoset injection molding process by image texture analysis, *Advanced Manufacturing: Polymer & Composites Science*, 8:1, 22-32, DOI: [10.1080/20550340.2022.2033905](https://doi.org/10.1080/20550340.2022.2033905)

To link to this article: <https://doi.org/10.1080/20550340.2022.2033905>



© 2022 The Author(s). Published by Informa UK Limited, trading as Taylor & Francis Group.



Published online: 07 Feb 2022.



Submit your article to this journal [↗](#)



Article views: 128



View related articles [↗](#)



View Crossmark data [↗](#)

Study of material homogeneity in the long fiber thermoset injection molding process by image texture analysis

Robert Maertens^{a,b} , Ludwig Schöttl^a, Wilfried V. Liebig^a , Peter Elsner^{a,b} and Kay A. Weidenmann^c

^aKarlsruhe Institute of Technology KIT, Institute for Applied Materials - Materials Science and Engineering IAM-WK, Karlsruhe, Germany; ^bFraunhofer Institute for Chemical Technology ICT, Pfinztal, Germany; ^cAugsburg University, Institute for Materials Resource Management MRM, Hybrid Composite Materials, Augsburg, Germany

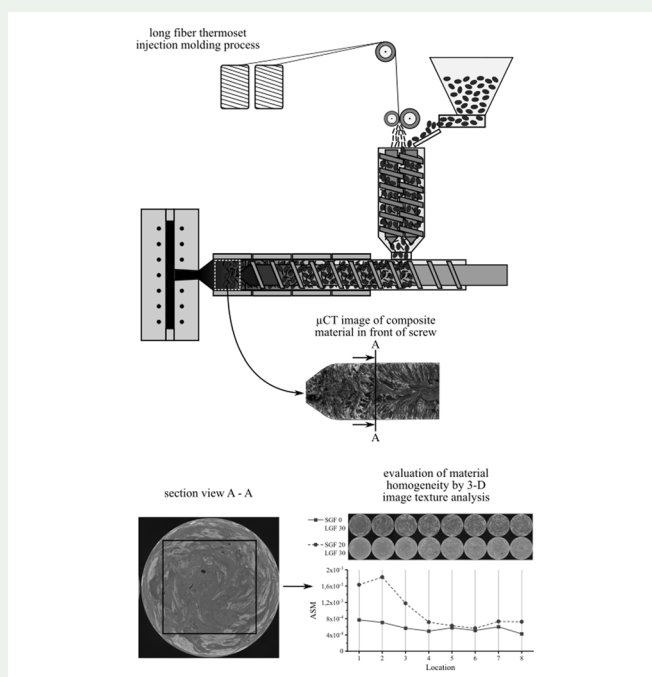
ABSTRACT

To quantify the homogeneity of fiber dispersion in short fiber-reinforced polymer composites, a method for image texture analysis of 3-dimensional X-ray micro computed tomography (μ CT) images is presented in this work. The adaption of the method to the specific requirements of the composite material is accomplished using a statistical region merging approach. Subsequently, the method is applied for evaluating the homogeneity of specimens from an intermediate step of the long fiber thermoset injection molding process as well as molded parts. This new injection molding process enables the manufacturing of parts with a flexible combination of short and long glass fibers. By using a newly developed screw element based on the Maddock mixing element design, the material homogeneity of parts molded in the long fiber injection molding process is improved.

KEYWORDS

Thermoset injection molding; Maddock screw mixing element; phenolic molding compound; long glass fiber; CT analysis; microstructural analysis; Haralick texture feature

GRAPHICAL ABSTRACT



1. Introduction

Composite parts manufactured from fiber-reinforced phenolic molding compounds have a high maximum operating temperature, an excellent chemical resistance, and a very good dimensional accuracy. These characteristics enable their application in the direct vicinity of the internal combustion engine

[1–3]. Recent developments have proven that phenolic molding compounds can successfully be used in electric motors for traction applications [4,5]. However, one of the biggest challenges for the wide use of phenolic resin molding compounds is their brittle deformation behavior [6,7]. For achieving good mechanical properties in a short fiber-

CONTACT Robert Maertens  robert.maertens@kit.edu  Karlsruhe Institute of Technology KIT, Institute for Applied Materials - Materials Science and Engineering IAM-WK, Engelbert-Arnold-Straße 4, 76131, Germany

© 2022 The Author(s). Published by Informa UK Limited, trading as Taylor & Francis Group.

This is an Open Access article distributed under the terms of the Creative Commons Attribution License (<http://creativecommons.org/licenses/by/4.0/>), which permits unrestricted use, distribution, and reproduction in any medium, provided the original work is properly cited.

reinforced polymer composite material, in general high average fiber lengths are important. Thomason and Vlugg noted a significant increase in tensile modulus of glass fiber-reinforced polypropylene up to a fiber length of $L = 1$ mm [8]. In a subsequent publication, Thomasson et al. found that the tensile strength of the same material system increases up to a fiber length of $L = 3$ mm ... 6 mm and levels out at higher length values [9]. Similar results were reported by Fu and Lauke [10]. They conclude that the strength of a short fiber-reinforced composite approaches a plateau level at mean fiber length values of $L > 5x L_c$. With their assumption of the critical fiber length L_c of approximately $L_c = 0.8$ mm ... 2.5 mm for various glass fiber reinforced thermoplastics, this corresponds to a fiber length range of $L = 4$ mm ... 12.5 mm which is required for obtaining the full reinforcement potential. Lastly, Kim and Park [11] found that the impact strength increases with the fiber length in their investigated fiber length range of $L = 0.5$ mm ... 2 mm. In addition to high average fiber length, a homogeneous distribution of the fibers in the polymer matrix is important as well [12–14]. The presence of fiber bundles is not desired, because they act as defects. Fiber bundles typically originate either from poorly melted long fiber granulate or from directly fed long fiber strands [14].

A newly developed injection molding process aims to increase the fiber length in the molded part compared to the state-of-the-art thermoset injection molding, in which mean fiber length values of $L = 0.3$ mm ... 0.35 mm are typical [15]. Thereby, the disadvantages of the phenolic molding compounds mentioned above shall be mitigated. The new process enables the manufacturing of phenolic resin parts with a tailored combination of long glass fibers (LGF) and short glass fibers (SGF) [16]. Previously conducted investigations have shown that the main processing challenge in the long fiber thermoset injection molding process is the opening of the fiber bundles and the dispersion of the long fibers in the thermoset matrix. In this research paper, the usage of a screw mixing element for increasing the material homogeneity is investigated. To quantify the effect of the mixing element on the homogeneity, a method for image texture analysis of 3-dimensional X-ray micro computed tomography (μ CT) images of the fiber-reinforced material is introduced and applied.

1.1. Mixing screw elements for the injection molding process

The compression-less conveying screw that is typically used in state-of-the-art thermoset injection

molding processes has a limited mixing capability and is mainly used for melting and pumping already homogeneous materials. If formulation constituents such as colorants [17,18], fiber bundles [12] and fillers [19] need to be homogenized in the polymer melt, a higher mixing power is required. Dispersive mixing by means of shear energy input can be achieved by forcing the molten polymer material through narrow gaps, either during the plasticizing or the injection phase of the process. For mixing elements on the injection molding screw, the same geometries are used in the continuous single-screw extrusion and the discontinuous injection molding process. Generally, desirable features for screw mixing elements according to Rauwendaal are listed below [20,21]

1. Forward pumping capability to minimize the pressure drop over the mixing section
2. Streamlined flow and a complete wiping of the barrel circumference to avoid dead spots and to achieve a narrow residence time distribution
3. Easy cleaning during material changeover and machine downtime

Due to their good compromise between ease of screw element manufacturing and mixing capabilities, the fluted mixing elements based on the Union Carbide/Maddock mixing geometry are commonly used for extrusion and injection molding applications and have been the focus of several investigations [17–28]. The Maddock mixing element consists of inlet and outlet flutes, which are separated by the shear flight. The polymer material enters the mixing element through the inlet flute. Since the inlet flute is closed towards the machine nozzle, the material is forced through the narrow gap between the screw element and the barrel into the outlet flute. This screw channel is open towards the machine nozzle, so that the material can exit the screw element in that direction.

The main influence factors on the mixing quality of a spiral Maddock element according to Potente and Többen [28] are the length of element, the helix angle and the shear gap geometry. Rauwendaal et al. [29] and Kubik et al. [30] investigated mixing element designs that subjected the material to more than one passage through a narrow shear gap and found a positive influence on the mixing element performance. They also investigated the effect of a wedge-shaped flank geometry, which creates elongational stress in addition to the shear stress. This is supposed to be better suited for breaking up agglomerates. While Rauwendaal et al. [29] found a positive influence, Kubik et al. [30] could not confirm this. Sun et al. [25,26] conducted numerical and

experimental investigations on the influence of the flute channel geometry and the shear gap height for Maddock screw mixing elements and found that a shallower flute depth results in a narrower residence time distribution, therefore reducing the potential of dead spots and material degradation.

The previously cited works used several different methods to evaluate the screw element mixing performance. During the screw element design phase, calculating the hydrodynamic forces on particles either analytically [29] or numerically [17] is common. Another numerical method implemented by Sun et al. [26] separates the polymer mass flow conceptually into two separate, but rheologically identical flows. Each flow is assigned tracer elements, whose displacement is tracked when the polymer flows through the mixing section.

Various experimental techniques for determining the mixing quality have been utilized. Essegir et al. [27] fed the single screw extruder with two immiscible fluids, prepared micrographs of the extrudate and subsequently measured the particle sizes of the two phases. Kubik et al. [17] used an inline melt camera system, which consist of a glass-window extruder section, a diffuse light source on one side of the polymer stream and a camera on the opposite side. The camera saves multiple gray value images at a fixed frame rate over a certain measurement time. Subsequently, the average and the standard deviation of the gray values over the measurement duration are calculated. A poor mixing performance results in images with high or low levels of particle dispersion. Consequently, this corresponds to a high standard deviation of the gray values.

No usage of a Maddock style mixing element in the thermoset injection molding process of phenolic resin molding compounds has been reported in the literature. In this research paper, the effect of a thermoset-specific Maddock mixing screw on the material homogeneity is presented. The design process for the screw element and the results are described in Section 3.1.

1.2. Image texture analysis

To quantify the effect of the newly developed Maddock screw mixing element and the material formulation on the material homogeneity, a method for image texture analysis of 3-dimensional X-ray micro computed tomography (μ CT) images of the plasticized fiber-matrix compound is presented in this work. The method development is introduced in detail in Section 2.4.

In general, gray value images can be described using two features: “Tone” and “texture”. The tone of an image describes the quantitative distribution

of the image’s gray values and can be visualized in a histogram. The spatial distribution of the gray values within the image is called the texture [31]. For quantifying the texture, Haralick et al. [32] proposed 14 different calculation methods, known as the Haralick texture features. One of these texture features, the angular second moment (ASM) represents the number of gray-tone transitions in an image [32]. In the first step for determining the texture features, the gray level co-occurrence matrices (GLCM) are calculated. They contain information about the relative frequencies P_{ij} with which two image cells, separated by the distance d , have the gray values i and j . For a 2-dimensional image, four GLCMs exist, one for each calculation direction (horizontal, vertical, diagonal, antidiagonal). The texture feature angular second moment (ASM) can be calculated according to Equation (1)

$$\text{ASM} = \sum_{i=1}^{N_g} \sum_{j=1}^{N_g} \left(\frac{P(i,j)}{R} \right)^2 \quad (1)$$

where R is the number of neighboring cell pairs, which is used for the normalization of the calculation results and N_g are the number of gray levels in the image. $P(i,j)$ are values of the entries of the GLCMs. The theoretical value range for the ASM spans from $1/N_g^2$ to 1 [33]. The lower boundary represents a transition between the extreme values of the gray levels for each pixel in the image, i.e. an image with the lowest possible homogeneity. A value of $\text{ASM} = 1$ represents a completely homogeneous, constant image. The ASM has been used as a measure for the homogeneity of an image by several authors in the context of aerial photography [34], chemistry [35,36] and medicine [37]. Within this work, it is the hypotheses that the ASM can be used for describing the homogeneity of a fiber-reinforced composite material.

For a homogeneous image, the GLCMs contain a small number of large entries $P(i,j)$. The sum of squares and therefore the ASM for the homogeneous image is high. The GLCMs for an inhomogeneous image have many small entries $P(i,j)$. Consequently, the sum of squares and therefore the ASM for the inhomogeneous image will be low.

The original 2-dimensional texture analysis by Haralick et al. has been transferred to a 3-dimensional calculation by several authors, simply by adding additional calculation directions without changing the fundamental principle. The transfer to 3-dimensional images is accomplished by calculating a higher number of GLCMs: Instead of four GLCMs, 13 must be calculated in the 3-dimensional case. From these GLCMs, the same texture features as in the 2-dimensional case can be determined. This has been applied for describing medical images

[38–41] and for evaluating the quality of food products [37].

In the original procedure described by Haralick et al., the GLCMs are calculated for neighboring cell pairs. Most studies using the texture features follow that calculation procedure. However, if an image with a characteristic pattern of a known size shall be characterized, a modification of the calculation distance can be useful. By using a calculation distance that is in the same magnitude as this characteristic pattern, the expressiveness of the results can be improved [42].

To the knowledge of the authors, the Haralick texture features have not been applied for image analysis characterization in the field of composite materials before, neither in the 2-dimensional nor in the 3-dimensional case. In this work, a method for quantifying the homogeneity of specimens manufactured in a long fiber thermoset injection molding process is introduced. Compared to the established methods for evaluating the mixing performance that are described in Section 1.1, this method offers the advantage of a complete, 3-dimensional consideration of the composite material.

2. Material and methods

2.1. Materials

The phenolic resin molding compound used for this study is based on the commercially available Vyncolit® X6952 [43] and was compounded by means of twin-screw extrusion. In the long fiber thermoset injection molding process, continuous glass fiber rovings (3B fibreglass 111AX11 [44]) were cut to a length of $L=5$ mm and fed directly into the plasticizing unit according to the process scheme described in the next section and depicted in Figure 1.

2.2. Long fiber thermoset injection molding process and screw element development

The newly developed long fiber thermoset injection molding process enables a flexible combination of short glass fibers (SGF) and long glass fibers (LGF) by separating the two mass flows. While the SGF are gravimetrically fed as a formulation constituent of the phenolic resin molding compound, the LGF are directly chopped from continuous fiber rovings and fed into the plasticizing unit of the injection molding machine. The injection molding screw is a compression-less conveying screw with an interchangeable screw tip, which allows the adaption of either a conventional conveying geometry or the newly designed, thermoset specific Maddock mixing element.

2.3. Image texture analysis method application

Two different kinds of specimens were obtained for this study: The plasticized compound in front of the screw and the molded parts. Their respective positions along the injection molding process route are marked in Figure 1. For judging the influence of the base material formulation on the fiber dispersion quality, the plasticized compound in front of the screw is analyzed. These specimens are called “group 1”. To obtain them, a stable injection molding process was stopped after the plasticizing step. The compound in front of the screw, which would have been injected into the mold in the next process step, was cooled down and removed from the barrel once it was solidified. The conveying screw tip was used. A PF-SGF0-LGF30 ($\varphi=0$ % SGF- and $\varphi=30$ % LGF-content by weight) and a PF-SGF20-LGF30 ($\varphi=20$ % SGF- and $\varphi=30$ % LGF-content by weight) formulation, both containing long glass fibers chopped to a length of $L=5$ mm, were investigated. One specimen per formulation was

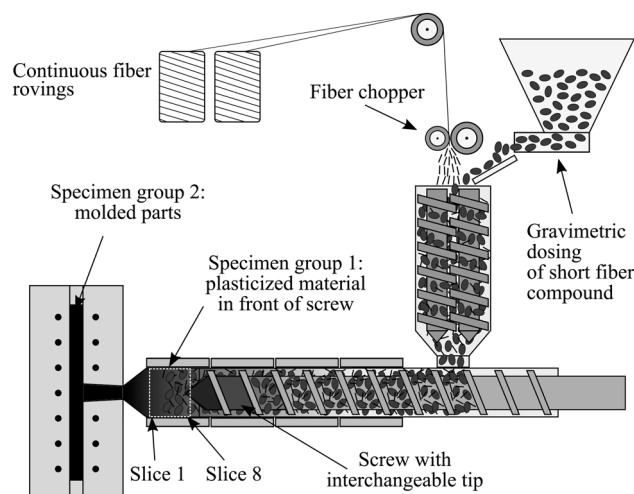


Figure 1. Process scheme long fiber thermoset injection molding process.

investigated, which results in a total number of two specimens for this group.

The second group of specimens was cut from molded plates. Here, the focus was not on the material formulation, but instead on the influence of the screw geometry and the process parameters on the fiber dispersion quality. Consequently, the same PF-SGF0-LGF30 formulation was used for all specimens within this group, but the screw geometry and the screw speed were varied in three steps: Conveying element, mixing element with screw speed 30 1/min and mixing element with screw speed 80 1/min. One specimen per process variation was investigated, which results in a total number of three specimens for this group.

The PF-SGF20-LGF30 formulation was not used for the investigations carried out with specimen group 2. Due to the high shear energy input by the mixing element and the overall higher fiber content of the PF-SGF20-LGF30 formulation, an overheating and consequently a premature curing of the phenolic resin occurred, making it impossible to reliably mold parts.

Images of all specimens were subsequently acquired by using a XYLON precision μ CT with the image acquisition parameters listed in Table 1.

The choice of the voxel size is a compromise between the image resolution and the specimen volume that can be investigated. The glass fibers that were used for the present study have a diameter of $d_f = 17 \mu\text{m}$ [44], which means that individual fibers cannot be detected. However, considering that the long glass fiber roving weight of 2400 tex corresponds to a fiber count of approximately $n = 4000$ fibers per roving, the chosen voxel size is deemed sufficiently small to detect fiber bundles.

2.4. Image texture analysis method development for evaluating material homogeneity

In the following section, the specific adaption of the Haralick texture feature calculation to the requirements of the composite material and the specimen's geometry is described. For all specimens, the μ CT-images are resliced and cropped to a cuboid size. This was done to exclude the air around the edges of the specimens from the calculation. Next, the images are converted to an 8-bit gray level format

and smoothed to reduce the noise level. The smoothing was carried out using the default algorithm in the software ImageJ [45], which replaces each voxel with the average of the $3 \times 3 \times 3$ neighborhood [46]. Preliminary investigations had shown that the smoothing step increases the ASM value difference between a homogeneous and an inhomogeneous image, which increases the expressiveness of the results. This is visualized in Figure 2, which gives exemplary ASM calculation results for the exact same images both with and without the image smoothing process step. Figure 2 shall only visualize the difference caused by the application or the omission of the image smoothing. The physical significance of the results will be described and discussed in Sections 3.2 and 4.

By applying the image smoothing, the relative difference between the lowest and the highest ASM value increases from 115 % to 225 %, thus increasing the expressiveness of the results. For this reason, the image smoothing is applied for all texture feature calculations.

The approach of using multiple calculation distances followed by taking the average value for the ASM is applied. To select suitable calculation distances for generating the GLCMs, the characteristic regions of the image are examined. Figure 3 (left) shows a representative cross-section view of a μ CT image from a specimen of group 1. By using a statistical region merging algorithm [47] available for the software ImageJ [45], those distinct phases are merged to homogeneous regions as shown in Figure 3 (right).

The calculation distances for determining the GLCMs were defined by manually measuring typical sizes for regions containing fiber bundles and porosities. The measurements were carried out manually in multiple images using the “measure” function in the software ImageJ. Based on these sample measurements, size ranges from $s = 20$ voxels to $s = 60$ voxels (vx) were determined. For this reason, the calculation distances for determining the GLCMs in specimen group 1 are set to values of $d = 20 \text{ vx} = 940 \mu\text{m}$, $d = 40 \text{ vx} = 1880 \mu\text{m}$ and $d = 60 \text{ vx} = 2820 \mu\text{m}$. This corresponds to bundle sizes of several hundreds of fibers. Some fiber bundles still had the initial fiber length of $L = 5 \text{ mm}$. The identical

Table 1. Image acquisition parameters for μ CT scans.

Parameter	Unit	Value specimen group 1	Value specimen group 2
Tube head	–	Directional focus tube	
Target	–	Tungsten	
Acceleration voltage	kV	145	120
Tube current	mA	0.15	0.1
Voxel size	μm	47	36
Integration time	ms	500	750
Frame binning	–	2	1

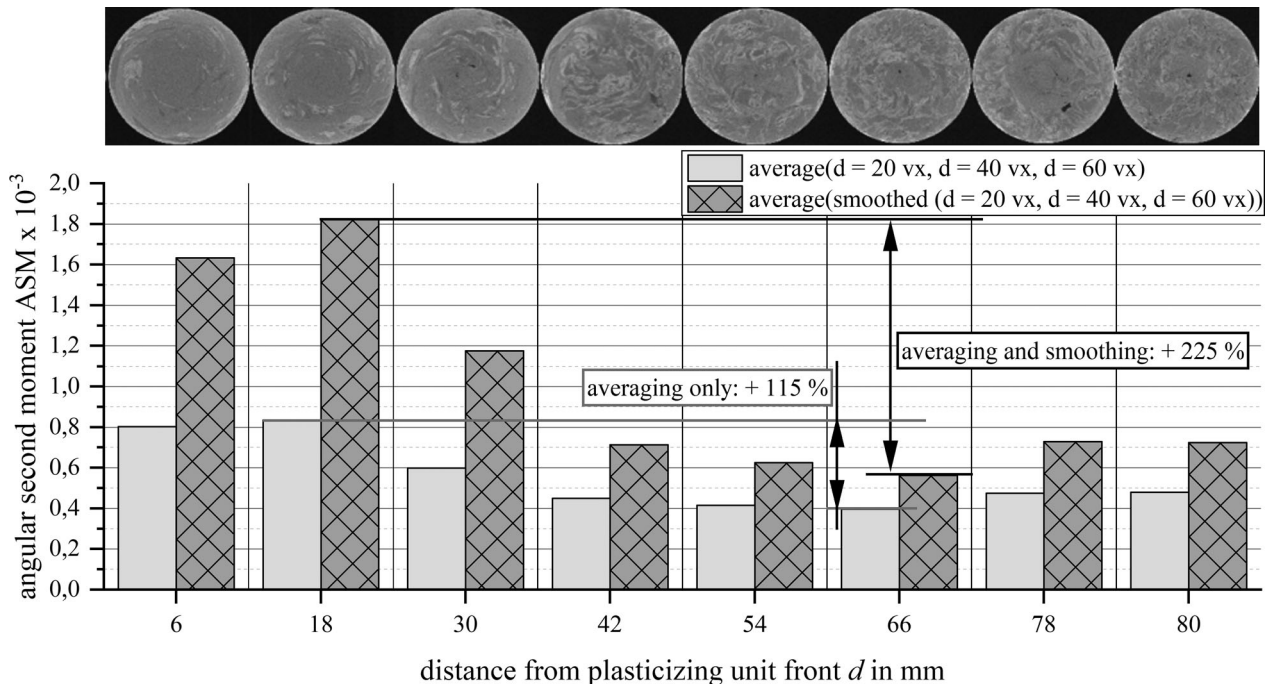


Figure 2. Effect of smoothing during image processing on the expressiveness of the results.

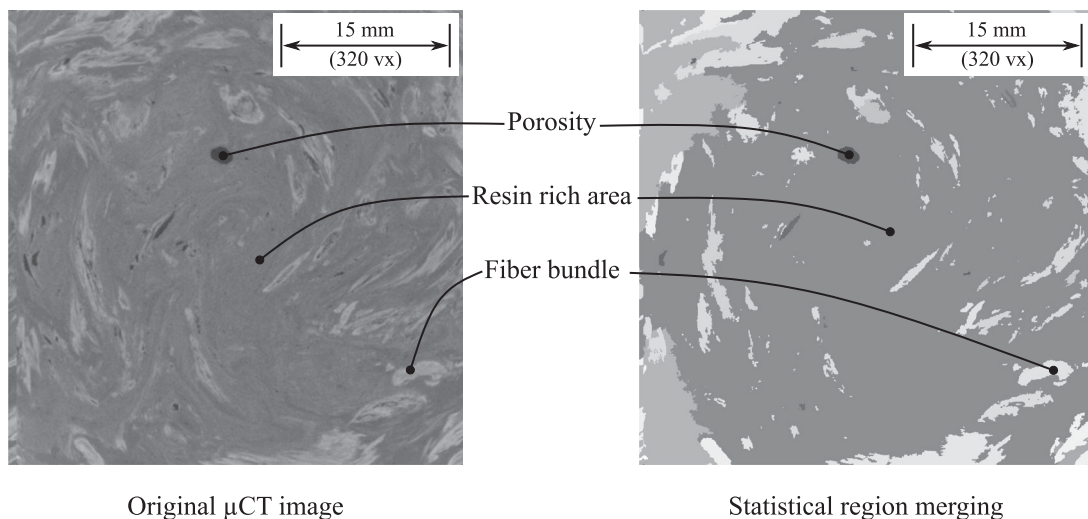


Figure 3. μ CT image before (left) and after (right) statistical region merging processing step.

procedure for specimen group 2 led to calculation distances of $d = 50$ vx, $d = 100$ vx and $d = 150$ vx.

For each individual image, one GLCM per calculation orientation per calculation distance is created. In the present case of a 3-dimensional image with 3 calculation distances, this results in $n = 13 \times 3 = 39$ GLCMs per slice. For each GLCM, the corresponding ASM values are calculated according to Equation (1). The three ASM values for the three calculation distances for each individual image are subsequently averaged to obtain a single resulting value per image, which is then used for the further analysis. The calculation procedure was

implemented in the software ImageJ by using the Ops framework [48, 49].

To be able to identify spatial differences in the homogeneity within the two specimens, the cuboid images of specimen group 1 are sliced into smaller images with a height of $h = 250$ vx each. This results in eight slices for each of the two specimens, with the first slice being positioned towards the machine nozzle and slice number eight located towards the screw of the injection molding machine. The slice position is marked in Figure 1. Due to their overall smaller size, no slicing was conducted for the specimens of group 2.

3. Results

3.1. Maddock screw mixing element design results

The thermoset-specific screw mixing element that was designed for the long fiber thermoset injection molding process has three distinct differences compared to a traditional Maddock mixing element for thermoplastic materials, which are derived from the literature information described in Section 1.1. Figure 4 (top) shows the thermoset-specific mixing element in direct comparison to the standard conveying screw geometry (Figure 4 bottom).

In contrast to a traditional Maddock mixing element for thermoplastic materials, the thermoset element has three distinct differences, which are derived from the literature information described in Section 1.1. First, the inlet channels feature a gradual slope at their ends to facilitate the flow of material and to avoid material accumulations. This feature is also designed for narrowing the residence time distribution by reducing the danger of material accumulations.

The second feature difference to the traditional Maddock mixing element is the edge fillet on the mixing flight. Due to the radius on this edge, the material must undergo additional elongational stresses when passing through the shear gap. This reflects the findings by Rauwendaal [29] regarding the mixing effect of elongational stresses.

The third main feature is that the positions of the mixing flight and wiping flight are reversed compared to the state-of-the-art. Figure 5 explains this difference by depicting cross-sections of a conventional Maddock element (left) and the new thermoset-specific design (right). The direction of the flow of material through the shear gap is marked for both elements.

Traditionally, the pushing flank is simultaneously also the wiping flank of the mixing element. This

makes sense for thermoplastic materials that enter the mixing element in a completely molten state. However, this condition does not apply for thermoset injection molding. Due to the low shear screw design, the thermoset molding compounds only start to melt in the foremost screw flights under the influence of pressure. This pressure is transferred into the molding compound by the screw flanks of the conveying screw, which means that the material close to the pushing screw flanks is molten, whereas the material distant from the screw flanks might still be granular [50]. If the molding compound entered a traditional mixing element in such a state, the granular fraction would be pushed through the shear gap, likely blocking it. The thermoset-specific design developed here ensures that only molten material is pushed through the shear gap, thus avoiding a blockage.

3.2. Material homogeneity investigations

Figure 6 shows the ASM calculation results for the first group of specimens.

The PF-SGF0-LGF30 formulation has a low homogeneity, which can be recognized by the white fiber bundles in the images shown in Figure 6 and the low ASM value. In contrast, the PF-SGF20-LGF30 formulation is more homogeneous, especially towards the machine nozzle at the front of the plasticizing unit. Both the differences within the individual specimen as well as between the two specimens are represented by the calculated image texture feature ASM. The fiber content has been verified using thermogravimetric analysis at $T = 650\text{ }^{\circ}\text{C}$ for $t = 36\text{ h}$. For all specimens, no relevant deviations of the actual fiber content from the set fiber content was found.

Although the identical material formulations for specimen groups 1 and 2 were used, a direct comparison of the calculated ASM values is not possible

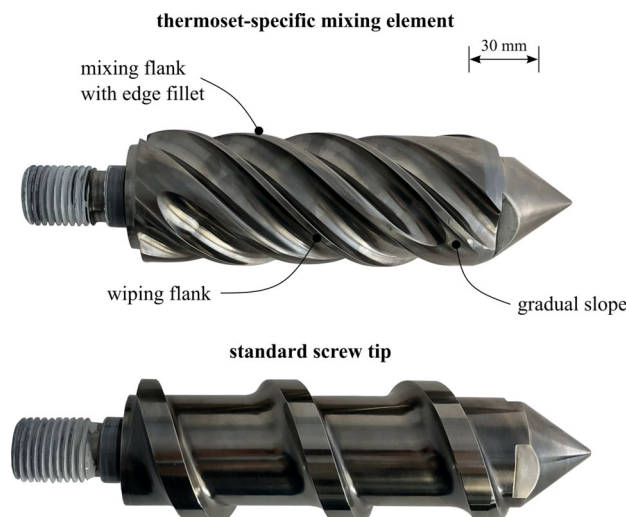


Figure 4. Thermoset-specific Maddock mixing element (top) and standard screw tip (bottom).

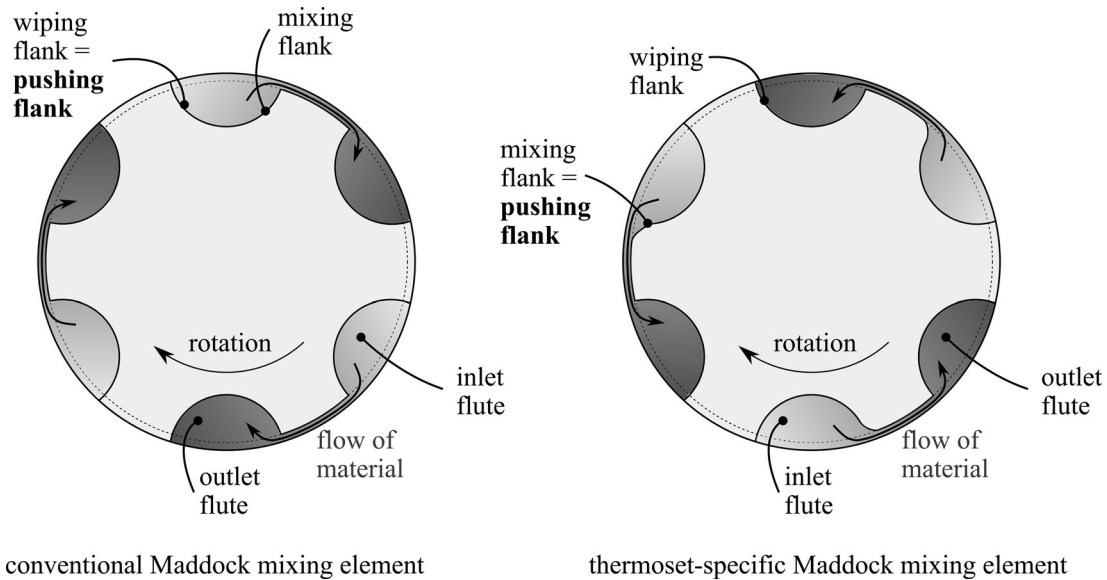


Figure 5. Position of mixing flank and wiping flank for the thermoset Maddock mixing element.

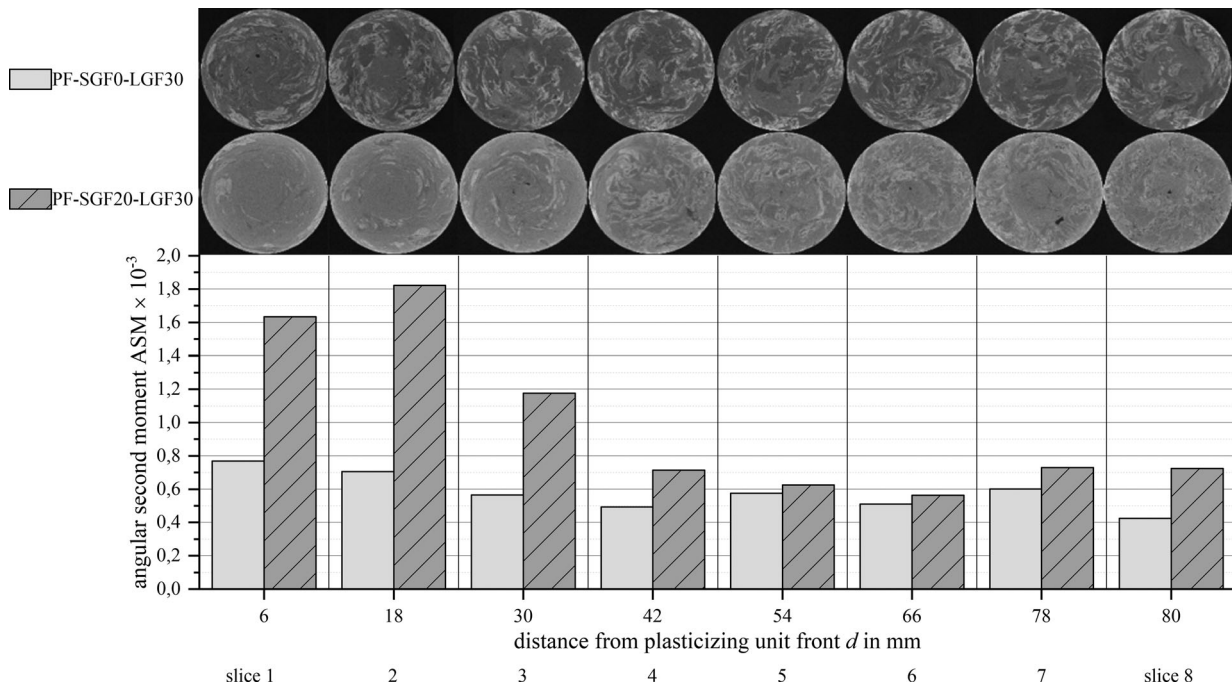


Figure 6. ASM calculation results for PF-SGF0-LGF30 and PF-SGF20-LGF30 formulations.

for multiple reasons. The group 1 specimens consist of resin rich areas, fiber bundles and voids. In contrast, the specimens from group 2 were molded under the influence of the high in-mold pressure. Consequently, they do not show any voids and consist only of two phases (resin rich areas and fiber bundles). Furthermore, the image acquisition parameters (Table 1) had to be adapted to achieve high-quality images.

The ASM results for the molded parts (specimen group 2) are shown in Figure 7. Additionally, representative cross-sectional images are depicted. The visual impression of the images clearly indicates a

higher homogeneity for the parts molded with the mixing element. The corresponding ASM values are higher for the parts molded with the mixing element and for the higher screw speed.

4. Discussion

The results for specimen group 1, the plasticized material in front of the screw, show that an overall higher fiber content leads to a higher material homogeneity. In general, the viscosity of a fiber-reinforced polymer material increases with increasing fiber and filler content [51]. Therefore, it can be assumed that

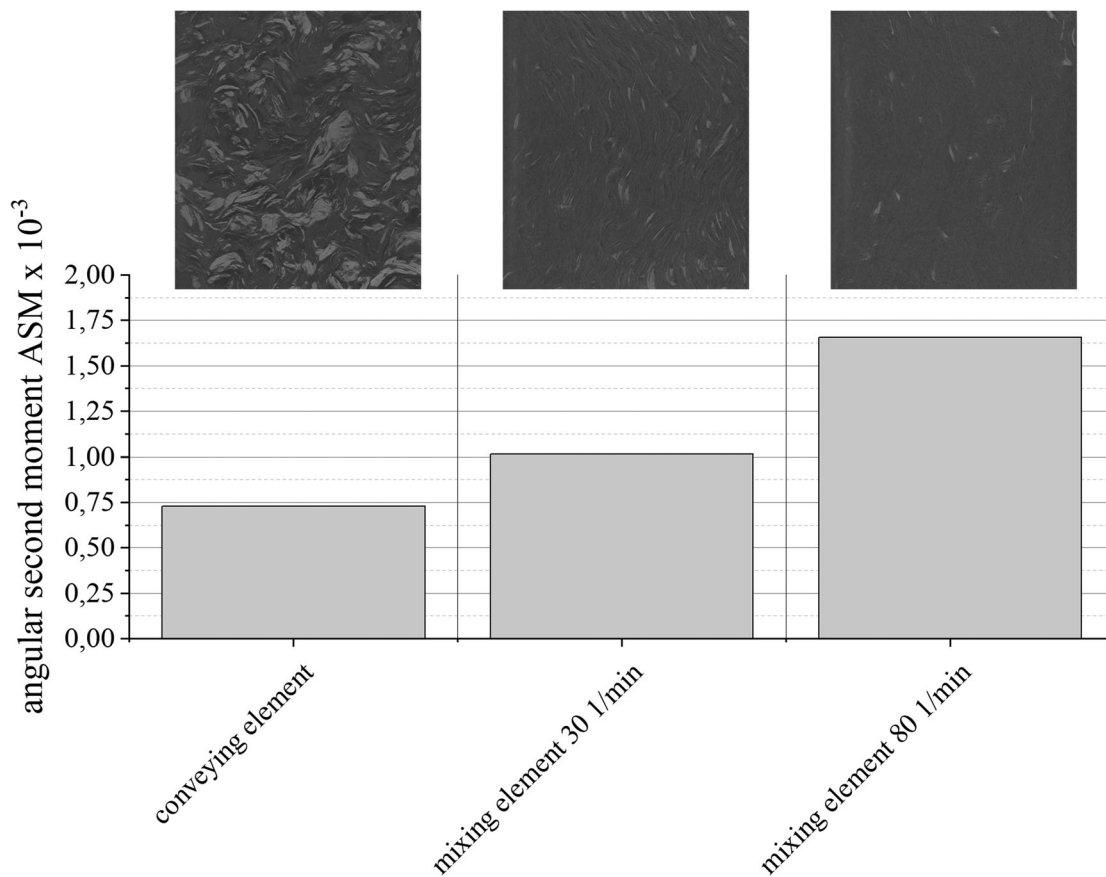


Figure 7. ASM values for PF-SGF0-LGF30 formulation process parameter variations.

the PF-SGF20-LGF30 material has a higher viscosity than the PF-SGF0-LGF30 formulation. The increased viscosity has two effects on the thermoset injection molding process. First, it leads to a higher shear energy input while plasticizing action in the injection molding screw. Second, it results in a higher required injection pressure for pushing the compound through the machine nozzle and into the mold.

The first aspect serves as an explanation for the overall higher level of inhomogeneity in the PF-SGF0-LGF30 specimen. Since the shear energy input for this formulation is lower, less fiber bundles are opened. The second aspect, the higher required injection pressure, creates a larger amount of backflow during the injection phase, which contributes to the better mixing and consequently the higher homogeneity in the front parts (slices 1-3) of the PF-SGF20-LGF30 specimen compared to its rear section (slices 5-8). Both aspects are visible in the illustrative images in [Figure 6](#) and are represented by the calculated ASM values.

The results for the molded parts (specimen group 2) show that the newly developed thermoset Maddock mixing element has a positive influence on the material homogeneity. By using the mixing element, both the number and the size of the fiber bundles are reduced, resulting in a more even and therefore more homogeneous distribution of the fibers in the polymer matrix. Again, this visual impression of the cross-

section view is in accordance with the calculated, quantitative ASM results. The screw speed has a linear correlation to the shear rate in the shear gap between the screw and the barrel [27]. Consequently, the molding compound that was plasticized with the higher screw speed contains less fiber bundles, which in turn results in a higher homogeneity of the molded part.

For all investigations, the calculation of the ASM confirms the visual impressions. Using the image texture analysis method to determine the homogeneity has the inherent advantage that the entire image stack in all three dimensions is considered for the calculation. The calculation procedure provides a single numerical value for an image, which enables simple and quick comparisons between multiple images or image slices. However, the reduction of a 3-dimensional image into a single numerical value is always accompanied by a loss of information. For example, the ASM does not contain any information about the shape or type of inhomogeneities. It simply returns a value for the homogeneity of the image. Additional information needs to be obtained by visual inspection of the image or the calculation of other texture features.

5. Conclusion

This work introduces an image texture analysis method which enables the quantitative evaluation of

the homogeneity of fiber-reinforced polymer composite materials. The 3-dimensional calculation of the image texture feature angular second moment (ASM) has been adapted to the requirements of the specimens produced in the long fiber thermoset injection molding process. By changing the two main method parameters – the calculation distance and the slicing of the images – the method was applied to two separate group of specimens which were produced in the long fiber thermoset injection molding process.

It was found that an increased glass fiber content in the composite material formulation leads to a higher homogeneity of the plasticized material in front of the injection molding screw, likely due to the higher compound viscosity. By using a newly developed screw mixing element, the homogeneity of the molded parts was improved compared to the conventional conveying screw geometry. A higher screw speed leads to an increased homogeneity when using the mixing element.

Based on the findings of the study described here, a more detailed trial series with material variations (total fiber content, SGF/LGF-ratio, fiber length) as well as process parameter variations (screw design, screw speed) has been conducted. The results will be presented in subsequent publications.

Acknowledgments

Raw materials: The phenolic molding compound was provided by Sumitomo Bakelite Co., Ltd. (Vyncolit N.V., Gent, Belgium).

We acknowledge support by the KIT-Publication Fund of the Karlsruhe Institute of Technology.

Disclosure statement

No potential competing interest was reported by the authors.

Funding

This work is funded by the Deutsche Forschungsgemeinschaft (DFG, German Research Foundation) projects EL 473/9-1 and WE 4273/18-1.

ORCID

Robert Maertens  <http://orcid.org/0000-0003-1449-7006>
 Wilfried V. Liebig  <http://orcid.org/0000-0003-1855-6237>

References

- Beran T, Hübel J, Maertens R, et al. Study of a polymer ejector design and manufacturing approach for a mobile air conditioning. *Int J Refrig*. 2021; 126:35–44.
- Jauernick M, Pohnert D, Kujawski W, et al. Hybrid lightweight cylinder crankcase: challenges and feasibility. *MTZ Worldw*. 2019;80(12):70–75.
- Schindele K, Sorg T, Hentschel T, et al. Lightweight camshaft module made of high-strength fiber-reinforced plastic. *MTZ Worldw*. 2020;81(9):26–31.
- Langheck A, Reuter S, Saburow O, et al. Evaluation of an integral injection molded housing for high power density synchronous machines with concentrated single-tooth winding. *2018 8th International Electric Drives Production Conference (EDPC) 2018*. 187–192.
- Reuter S, Keyser HD, Doppelbauer M. Performance study of a PMSM with molded stator and composite housing with internal slot cooling – resulting in high continuous power. *VDI Berichte*. 2020;2373: 17–31.
- Gardziella A, Pilato LA, Knop A. Phenolic resins: chemistry. Applications, standardization, safety and ecology. 2nd ed.; Berlin: Springer; 2000.
- Koizumi K, Charles T, Keyser HD. Phenolic molding compounds. In: Pilato LA, editor. *Phenolic resins: a century of progress*. Berlin: Springer; 2010. p. 383–437.
- Thomason JL, Vlug MA. Influence of fibre length and concentration on the properties of glass fibre-reinforced polypropylene: 1. Tensile and flexural modulus. *Compos A: Appl Sci Manuf*. 1996;27(6): 477–484.
- Thomason JL, Vlug MA, Schipper G, et al. Influence of fibre length and concentration on the properties of glass fibre-reinforced polypropylene: Part 3. Strength and strain at failure. *Compos A: Appl Sci Manuf*. 1996;27(11):1075–1084.
- Fu S-Y, Lauke B. Effects of fiber length and fiber orientation distributions on the tensile strength of short-fiber-reinforced polymers. *Compos Sci Technol*. 1996;56(10):1179–1190.
- Kim Y, Park OO. Effect of fiber length on mechanical properties of injection molded Long-Fiber-Reinforced thermoplastics. *Macromol Res*. 2020; 28(5):433–444.
- Truckenmüller F. Direct processing of continuous fibers onto injection molding machines. *J Reinf Plast Comp*. 1993; 12:624–632.
- Moritzer E, Budde C, Albring E. Fiber length reduction and homogeneity of injection-molded short fiber reinforced thermoplastics with special regard to the influence of a static mixing nozzle. In *ANTEC*. 2012. Orlando, FL: Society of Plastics Engineers. p. 1487–1493.
- Franzén B, Klason C, Kubát T, et al. Fibre degradation during processing of short fibre reinforced thermoplastics. *Compos*. 1989;20(1):65–76.
- Maertens R, Hees A, Schöttl L, et al. Fiber shortening during injection molding of glass fiber-reinforced phenolic molding compounds: Fiber length measurement method development and validation. *Polym.-Plast. Tech. Mat*. 2021;60(8):872–885.
- Maertens R, Liebig WV, Elsner P, et al. Compounding of short fiber reinforced phenolic resin by using specific mechanical energy input as a process control parameter. *J Compos Sci*. 2021;5(5): 127.
- Kubik P, Vlcek J, Tzoganakis C, et al. Method of analyzing and quantifying the performance of mixing sections. *Polym Eng Sci*. 2012;52(6):1232–1240.

18. Verbraak CPJM, Meijer HEH. Screw design in injection molding. *Polym Eng Sci.* 1989;29(7):479–487.
19. Wang Y, Huang J-S. Single screw extrusion compounding of particulate filled thermoplastics: State of dispersion and its influence on impact properties. *J Appl Polym Sci.* 1996;60(11):1779–1791.
20. Rauwendaal C. The ABC's of extruder screw design. *Adv Polym Technol.* 1989;9(4):301–308.
21. Rauwendaal C. *Polymer extrusion*. 5th ed. Hanser: München, 2014.
22. Tadmor Z, Klein I. Design of certain fluted mixing sections of extruder screws. *Polym Eng Sci.* 1973;13(5):382–389.
23. Elbirli B, Lindt JT, Gottgetreu SR. Analysis of the performance of maddock head mixer. In ANTEC. Chicago, IL: Society of Plastics Engineers; 1983.
24. Rauwendaal C. Design of fluted mixing sections. In ANTEC. New Orleans, LA: Society of Plastics Engineers; 1984.
25. Sun X, Gou Q, Spalding MA, et al. Maddock-style mixers for single-screw extrusion. In ANTEC 2017. Anaheim, CA: Society of Plastics Engineers; 2016. p.898–904.
26. Sun X, Spalding MA, Womer TW, et al. Design optimization of maddock mixers for Single-Screw extrusion using numerical simulation. In ANTEC 2017. Anaheim, CA: Society of Plastics Engineers; 2017, p 1017–1023.
27. Esseghir M, Gogos CG, Yu D-W, et al. A comparative study on the performance of three single-screw elements in melt-melt mixing of immiscible blends. *Adv Polym Technol.* 1998;17(1):1–17.
28. Potente H, Többen WH. Improved design of shearing sections with new calculation models based on 3D Finite-Element simulations. *Macromol Mater Eng.* 2002;287(11):808–814.
29. Rauwendaal C, Gramann P, Davis BA. New dispersive mixers for single screw extruders. In ANTEC 1998. Atlanta, GA: Society of Plastics Engineers; 1998.
30. Kubik P, Zatloukal M, Asai Y, et al. Experimental and numerical analysis of performance of two fluted mixer designs. *Plast Rubber Compos.* 2014;43(10):337–346.
31. Russ JC, Neal FB, *The image processing handbook*. 7th ed. Boca Raton, FL: CRC Press; 2018.
32. Haralick RM, Shanmugam K, Dinstein I. Textural features for image classification. *IEEE Trans. Syst., Man, Cybern.* 1973;3:610–621.
33. O'Byrne M, Ghosh B, Pakrashi V, et al. Texture analysis based detection and classification of surface features on ageing infrastructure elements. In Caprani C, O'Connor A, editors. *Proceedings of bridge and concrete research in Ireland conference*. Dublin, Ireland: Bridge and Concrete Research in Ireland. 2012. p. 223–228.
34. Connors RW, Trivedi MM, Harlow CA. Segmentation of a high-resolution urban scene using texture operators. *Comput Vision, Graph, Image Process.* 1984;25(3):273–310.
35. da Silva NC, Moura França L, de Amigo JM, et al. Evaluation and assessment of homogeneity in images. Part 2: Homogeneity assessment on single channel non-binary images. Blending end-point detection as example. *Chemom. Intell. Lab. Syst.* 2018;180:15–25.
36. Moura França L, de Amigo JM, Cairós C, et al. Evaluation and assessment of homogeneity in images. Part 1: Unique homogeneity percentage for binary images. *Chemom. Intell. Lab. Syst.* 2017;171:26–39.
37. Ávila M, Caballero D, Antequera T, et al. Applying 3D texture algorithms on MRI to evaluate quality traits of loin. *J Food Eng.* 2018;222:258–266.
38. Tesar L, Smutek D, Shimizu A, et al. 3D extension of haralick texture features for medical image analysis. In *Proceedings of the Fourth IASTED International Conference on Signal Processing, Pattern Recognition, and Applications*, Innsbruck. Anaheim: Acta Press; 2007.
39. Tesar L, Shimizu A, Smutek D, et al. Medical image analysis of 3D CT images based on extension of haralick texture features. *Comput Med Imaging Graph.* 2008;32(6):513–520.
40. Showalter C, Clymer BD, Richmond B, et al. Three-dimensional texture analysis of cancellous bone cores evaluated at clinical CT resolutions. *Osteoporos Int.* 2006;17(2):259–266.
41. Han F, Wang H, Zhang G, et al. Texture feature analysis for computer-aided diagnosis on pulmonary nodules. *J Digit Imag.* 2015;28(1):99–115.
42. Connors RW, Harlow CA. A theoretical comparison of texture algorithms. *IEEE Trans. Pattern Anal. Machine Intell.* 1980;2:204–222.
43. Sumitomo Bakelite Europe n.v. Technical Data Sheet X6952 green [cited 11 Nov. 2019]. Available from: <https://www.sbhpp.com/products-applications/catalog/item/vyncolit-x6952..>
44. 3B Fibreglass. Technical Data Sheet Direct Roving 111AX11.
45. Schindelin J, Arganda-Carreras I, Frise E, et al. Fiji: an open-source platform for biological-image analysis. *Nat Methods.* 2012;9(7):676–682.
46. User Guide IJ [cited 21 Dec. 2021]. Available online: [https://imagej.nih.gov/ij/docs/guide/146-29.html#sub.Smooth-\[S\]\(\)](https://imagej.nih.gov/ij/docs/guide/146-29.html#sub.Smooth-[S]()).
47. Nock R, Nielsen F. Statistical region merging. *IEEE Trans Pattern Anal Machine Intell.* 2004;26(11):1452–1458.
48. Rueden C, Dietz C, Horn M, et al. *ImageJ Ops*, 2016.
49. Graumann A, Dietz C. *ImageJ implementation of haralick texture features*. Konstanz, Germany: University of Konstanz; 2021.
50. Singh R, Chen F, Jones FR. Injection molding of glass fiber reinforced phenolic composites. 2: Study of the injection molding process. *Polym Compos.* 1998;19(1):37–47.
51. Osswald TA, Rudolph N. *Polymer rheology: fundamentals and applications*. Munich: Hanser; 2014.